F 1 Neutron Imaging

M. Strobl
Head of Neutron Imaging and Applied Materials Group (NIAG)
Laboratory for Neutron Scattering and Imaging
Paul Scherrer Institut, Villigen, Switzerland

Contents

Lecture Notes of the 50th IFF Spring School "Scattering! Soft, Functional and Quantum Materials"

Introduction

In contrast to other neutron scattering methods, neutron imaging assesses structures and processes with real space resolution on macroscopic length scales [1,2]. In general neutron imaging utilizes the same neutron interactions with matter as used by scattering techniques. Hence, the same qualities of neutron radiation are exploited such as

(i) **good transmission** for many materials, in particular structural materials,
(ii) **high sensitivity to some light elements** and especially hydrogen,
(iii) **isotope sensitivity** with an outstanding example amongst others being hydrogen and deuterium, enaling particularly **contrast variation**,
and last but not least
(iv) the **match of wavelength and energy** in the thermal range with **crystallographic distances and excitations**
(v) the **magnetic moment** of the neutron providing sensitivity to magnetic fields and strcutures.

Correspondingly neutron imaging has a wide range of applications in particular for scientific problems and non-destructive testing where x-ray imaging fails and the above characteristics are required.

An outstanding example being extensive studies in material science and industrial research&development (R&D) in the first two decades of the millenium that helped enable market readiness of commercial fuel cells (Fig. 1)[3-6]. Here several of the above mentioned advantages of neutrons are exploited. Neutrons penetrate the metallic casing of fuel cells, still being very sensitive to the water distribution, which can hence be probed in operando in real operational fuel cells. In order to understand the exchange of water in continuously wet areas of the cell Deuteration has been used, exploiting the isotope contrast. Lately even the use of polarized neutrons has been considered to simultaneously assess current flows within operational cells.

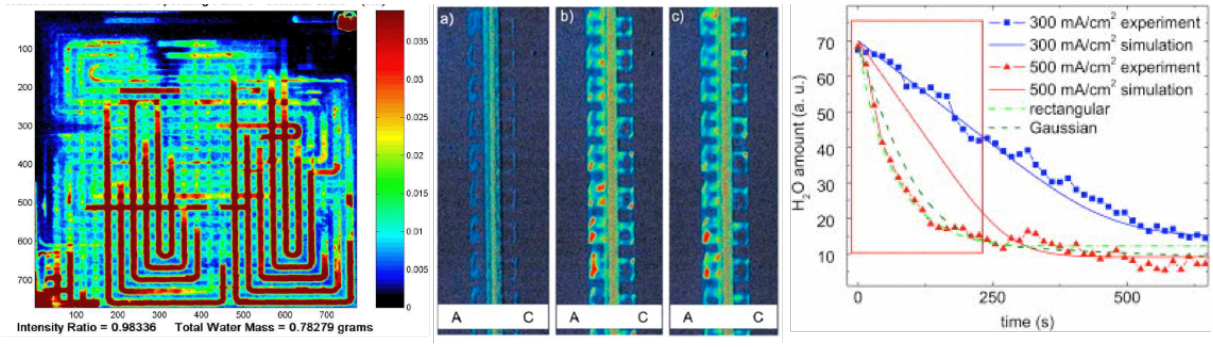

Fig. 1: In operando fuel cell studies mainly focussed on the water balance critical to the performance of fuel cells. The figure left gives an example of a through plane investigation of a full blown fuel cell in operation, displaying on the first glance the distribution of the produced water in the gas supply channels; More details with high spatial resolution are shown in the in-plane images in the middle, displaying individual channels as well as the membranes and gas diffusion layers in between; Finally, on the right hand side a quantification and modelling result deduced from studies utilizing H_2O/D_2O isotope contrast. It underlines further that the images

presented rarely are the results of a study but data at an intermediate reduction state finally serving quantitative measurements and modelling. In the specific case it has been found that at higher load the water management cannot be described anymore by a simple two phase flow model, but a discrete, eruptive transport model had to be developed based on the data;

Latest since the introduction of digital detectors for neutron imaging, one has to distinguish between different fundamental imaging modes with respect to the resolved dimensions. While initially, when images where recorded on film, only

- **2-dimensional projection imaging** was available, the digital data recording enabled an extension first to
- **3 dimensions**, either
  (i) **3D tomographic volumes** or
  (ii) **time resolved imaging** combining two spatial dimensions with the time dimension. Latest developments of acquisition technology enables
- **4D imaging**, namely time-resolved tomography, with latest reports having 3 sec time resolution for full 3D tomographies, enabling to observe processes real time in 3 dimensions.
- Taking into account techniques reconstructing 3D vector fields, the dimensionality of resulting data volumes is meanwhile ranging **up to 6D and beyond**.

Currenlty best **resolution**s achieved range down to below **5 μm in 2D imaging** and around **10 μm in 3D** imaging. Best time resolutions provide movies of processes with around **1000 frames per second**, and in so-called strobo-kinetic measurements, that image repetitive processes avergaing over a number of cycles, time resolution in the **microsecond range** are reported. Time resolved tomographies have been performed with **below 10 seconds per tomography** and spatial resolutions then ranging at few 100 μm. Note that spatial resolution is not to be confused with pixel resolution. In the ideal case the spatial resolution, which is defined as the full width at half maximum (FWHM) of the pointspread or at 10% modulation transfer in the reciprocal unit of line pairs per length, is at bbest twice the actual pixel size.

1 Neutron Imaging – Spatial Resolution

A general imaging experiment requires both, spatial resolution and contrast. While we will deal with the different contrast mechanisms in the next section, here we shall focus on spatial resolution.

Contrary to the wide spread believe that the spatial resolution capability of neutron imaging builds upon a highly collimated low divergence beam, state-of-the-art neutron imaging instruments utilize highly divergent beams for efficient imaging of large objects. This misconception is largely based on the fundamental difference, that other methods view the beam as an integrated entity described by overall parameters like wavelength, wavelength spread, polarisation, divergence etc. This is justified by the nature of these measurements integrating parameters over the whole probed area, respectively volume. This is fundamentally different in imaging with instantaneous spatial resolution (in contrast to scanning methods). To provide an example of this issue, we consider the use of a velocity selector for scattering and imaging. The specification of such devices has it, that the beam divergence has an impact on the wavelength resolution provided. This is due to the geometry

of the functional components, basically absorbing radial lamella mounted prallel on a rotation axis, which itself is parallel to the beam. The lamellas are twisted such to enable passage of a specific velocity of neutrons at a certain operation frequency. Obviously the geometry for passage is optimized for a specific beam direction and hence differs for neutrons with angular deviations, which is adding to the wavelength spread of neutrons passing. While the specified wavelength resolution describes the conditions sufficiently for an integrated assessment of the beam, the divergence dependence leads to lateral shift of the central wavelength over a spatially extended beam at the detector, where the spatial extension is based on the initial divergence at the upstream velocity selector device. As a consequence, the local wavelength resolution on an imaging detector might have a better wavelength definition, but the nominal wavelength will shift laterally across the image. Hence, local beam parameters have to be evaluated on the imaging detector rather than the overall, in this case, wavelength and wavelength resolution of the whole beam.

1.1 Spatial resolution - Geometry

Without the availability of sufficient lenses for neutrons the spatial resolution capability of neutron imaging is limited by the applied pinhole camera approach (Fig. 2)[1]. In analogy to the camera obscura technique, but adapted to transmission imaging, the resolution capability is determined by a pinhole D on the radiation source side, the distance L from there to the sample and the distance l from the sample to the detector. The ratio L/D is referred to as the collimation ratio, which defines the divergence of the neutron beam at a point in the sample and hence the principle intrinsic resolution limitation, because the image blur d introduced by this geometry will depend only on the L/D ratio and the sample to detector distance l of individual measurements.

$$d = l/(L/D). \quad (1)$$

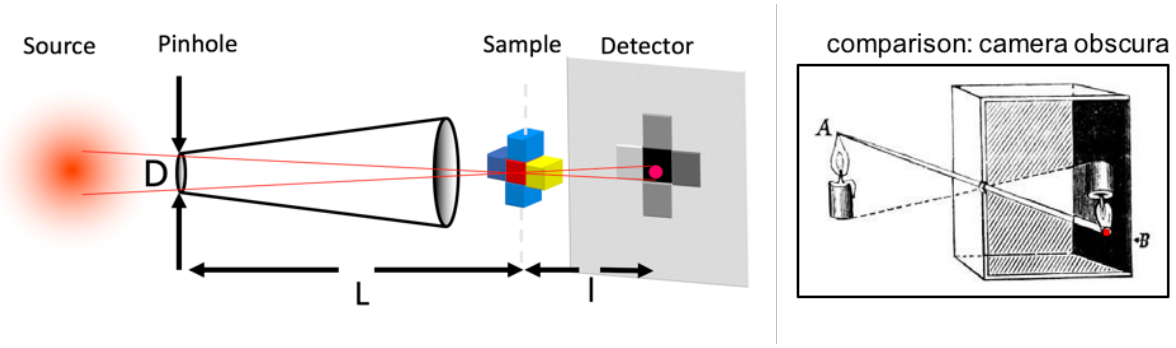

Fig. 2 Schematic of the pinhole imaging geometry of neutron imaging (left) and the analogy to the camera obscura principle (right); (red dots denote geometrical image blur)

From this it is obvious, that the most important measure to optimize results is to place samples always as close as possible to the detector, to minnimize the introduced image blur independent of other instrument parameters. Any other measure to improve the resolution capability in this geometry is a trade with instrument performance in terms of neutron flux. The parameters left to tune are the pinhole size D and the distance L, where modern instruments offer a variation of both within reasonable limitations. However, these impact the available flux density, as both the reduction of D and the increase L, while leading to improved resolution capabilities, lead to a reciprocal flux density decrease scaling with the

square of the collimation improvement, as can be seen easily, because they both impact 2 dimensions equally (note: flux density).

To further illustrate the limitations met in this respect, let's consider in an otherwise optimized set-up the attempt to improve resolution by a factor of two (in both dimensions, indeed!). Increasing *L/D* accordingly implies a flux density loss of a factor of four as discussed above. However, also the effective pixel size in the detection has to be reduced reciprocally by a factor of two, which is another factor of four in area. Hence, to achieve the same statistical significance an improvement of the resolution by a factor of two implies an increase in the required exposure by a factor of 16(!), i.e. more than an order of magnitude, which is not yet taking into account efficiency losses in the scintillator, when increasing the resolution requires optimizing the scintillator of a state-of-the-art detector. This has to be set in relation to maximum flux densities of the order of 10^8 n/cm^2/s achieved in the best state-of-the-art instruments.

Different approaches of overcoming this situation with neutron focussing devices (lenses) are discussed continuously and recently in particular an approach utilizing so-called Wolter Optics is considered by some to have significant potential for imaging applications [7]. However, to date no significant and reliable gains could be demonstrated and achieved, which would represent a distinct and broad relevance in the field.

1.2 Spatial resolution - Detector

Spatial resolution indeed depends intrinsically also on the ability of spatial detection resolution. With the flux limitations implied by spatial resolution of imaging outlined above, it must appear obvious that not only the spatial resolution capability, but with it also the efficiency of detection plays a crucial role for detectors and detection technology (Fig. 3).

The most utilized standard detector technology for neutron imaging is the scintillator/camera detector [1]. The advantages of this system compared to other digital detectors like e.g. amorphous silicon flat panels or microchannel plate(MCP)/medipix detectors [8] are the high quantum efficiency and particularly the high flexibility in trading spatial resolution and field of view (FOV) (Fig. 3), which are related to each other with respect to the total pixel number of the utilized camera chip. The detector system generally consists of a custom designed light tight box including a window covered by a specific scintillator, a mirror deflecting the light perpendicular out of the direct neutron beam towards the light optics and camera. Light optics (mostly commercial photographic lens systems), camera and scintillator can be exchanged straightforwardly according to the specific needs of individual measurements. Fields of view can vary within a range of about 0.5 x 0.5 m^2 to below 5 x 5 mm^2, corresponding effective pixel sizes from about 500 x 500 μm^2 to 1.5 x 1.5 μm^2. Scintillators of different sizes, thicknesses and materials can be attached. In general higher resolution requires thinner scintillator screens, with correspondingly opposite effects on efficiency and resolution capability (thicker scintillator screens imply up to a certain limit higher efficiency (detection probability), but also stronger blurring of the light output).

The main scintillator screen materials used are: LiF/ZnS where LiF acts as converter and ZnS as actual scintillation material for the secondary radiation from the capture by Li. Often the ZnS is doped, e.g. by Ag, to shift the wavelength of the emitted light to the range of the highest sensitivity of the used sensor chip. Mainly for high resolution also GADOX (Gd_2O_2S

– Gadulinium Oxysulfide) is used, which provides a higher capture probability essential for the thin screens for high resolution. The lower light output per neutron capture can even be an advantage for signal quality in the limit of low count rates. For extreme spatial resolutions (best currently in standard operation < 5 µm) even scintillators of isotope enriched ^{157}Gd have been developed and are utilized [9].

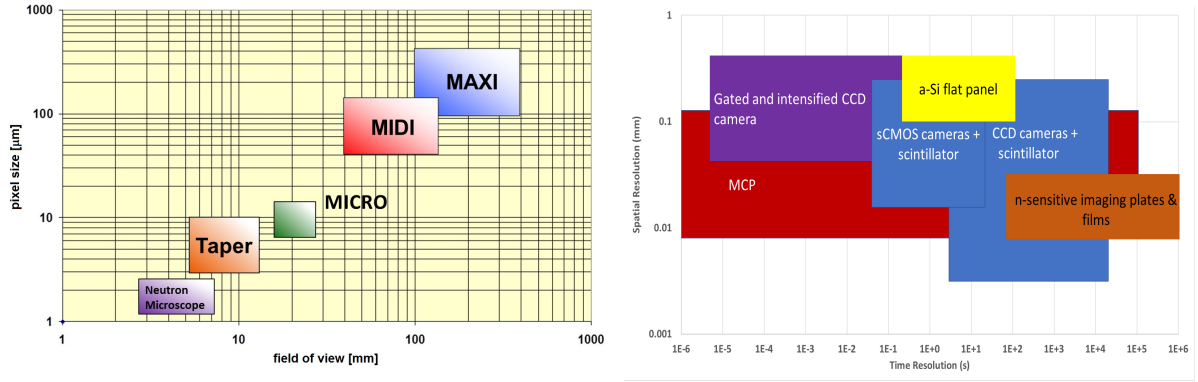

Fig. 3 Example of scintillator/camera imaging detector suite for various spatial resolution versus field-of-view requirements at NIAG at PSI, as well as an overview of utilized neutron imaging detectors in the context of spatial and temporal resolution;

Cameras utilized in neutron imaging feature CCD and CMOS technology with 1024 x 1024 up to 4096 x 4096 pixels. These are generally cooled in operation through air, water or Peltier cooling in order to enable low electronic noise. The choice of camera depends mainly on resolution, noise and exposure time consideration. These cameras are combined with state-of-the-art photographic optics, mostly focal lengths of about 50 mm and 100 mm are in use for large field of view and high resolution, respectively. For extreme resolutions more dedicated scientific optics enabling high light efficiency at high resolution are utilised [10,11].

In general the image detected by a camera detector $I_d(x,y)$ is affected by intrinsic detector noise I_{dc}, dominated by the dark current or read-out noise. An initial image correction is hennce simple background correction with an image I_{dc} recorded with closed shutters according to $I(x,z) = I_d(x,z) - I_{dc}(x,z)$.

Alternative detector solutions convey, but are not limited to, flat panel detectors, which provide digital images on relatively large fields of view, however, with limited resolution in the range of 100 µm, MCP/medipix detectors which provide resolutions down to around 10 µm, however with limited fields-of-view (FOV) of only around 10 cm^2 (Fig. 3). For some applications also film is used for image detection still, providing a unique combination of large fields of view and high spatial resolution, however, digitisation is tidious and prohibits time resolved and tomographic studies. Currently there is a large numer of imaging detector devlopments on the way, triggered mainly by the need for imaging detectors capable of time-of-flight resolution at pulsed neutron sources. In this endeavor the MCP/timepix detector can currently be regarded the benchmark, with some limitations, however, in FOV, count rate capability with respect to the last generation of spallation sources and long term stability for quantitative annalyses.

1.3 Three-dimensional spatial resolution - Tomography

Three dimensional spatial resolution of the internal structure of an object requires a tomographic approach. In general for measurements this implies that a significant number of projection images have to be recorded on an angular range of at least 180 degrees. In order to match the spatial resolution d achieved in the two dimensional transmission images, referred to as radiographies, the number of projections n required depends on the maximum radius of the object R with

$$n = (R/d)\pi/2 \tag{2}$$

The principle equation to retrieve cross section information from projections was derived by J. Radon [12] at the beginning of the 20th century. The basic transformation of a parallel beam tomography is, hence, named Radon transformation and written as

$$P(\theta,t) = \int\int f(x,y)\delta_D(xcos\theta + ysin\theta - t)dxdy \tag{3}$$

Here *f(x,y)* is the two dimensional function representing a slice of the sample which is projected into a number of one-dimensional functions *I(t)* at specific projection angles θ, with δ_D being the Dirac Delta function. Just like the equation and the term tomography implies three dimensional reconstructions are here based on stacking the reconstruction of two dimensional cross-sectional slices retrieved from the one-dimensional projection functions represented by single lines in the projection images, parametrized with *t*, while *x* and *y* are in the coordinate system of the sample.

To reconstruct the cross section *f(x,y)* one can explore a large number of paths. The simplest and most straight forward analytical reconstruction is direct backprojection as depicted in Fig. 4, left. In the simple backprojection, the intensities of the measured functions are smeared back onto a pixelated cross section according to their projection angle corresponding to

$$f'(x,y) = \frac{1}{n}\sum_{i=1}^{n} P(\theta_i, xcos\theta_i + ysin\theta_i) \tag{4}$$

Figure 4 illustrates, how adding a growing number of projections improves the reconstruction *f'(x,y)* of the slice. However, the right figure demonstrates more clearly the bias introduced through this simple approach particularly through the incomplete discrete sampling. The most applied reconstruction is hence a filtered backprojection algorithm. It correspondingly utilizes a filter in addition in order to even out the higher density in the center of the image as compared to the edges. The filter is applied in the frequency domain based on the Fourier slice theorem and in its most basic form has the shape $|\omega|$ where the Fourier transform reads

$$\hat{P}(\theta_i,\omega) = \int P(\theta_i,\omega)e^{-i2\pi\omega t}dt \tag{5}$$

and the filter is applied to the Fourier transformed projection $\hat{P}(\theta_i,\omega)$ as

$$P_f(\theta_i, \omega) = \int \hat{P}(\theta_i, \omega)\, e^{-i2\pi\omega t} |\omega| d\omega \tag{6}$$

which enables the backprojection of the filtered projection through

$$f'(x,y) = \frac{1}{n}\sum_{i=1}^{n} P_f(\theta_i, x cos\theta_i + y sin\theta_i) \tag{7}$$

A comparison of results of a simple shape with and without filtered back projection is shown in Fig. 4 on the right hand side and clearly underlines the requirement for filtering. In reality a number of different filters are used and are available in a wide range of reconstruction programs, commercially as well as freeware [13].

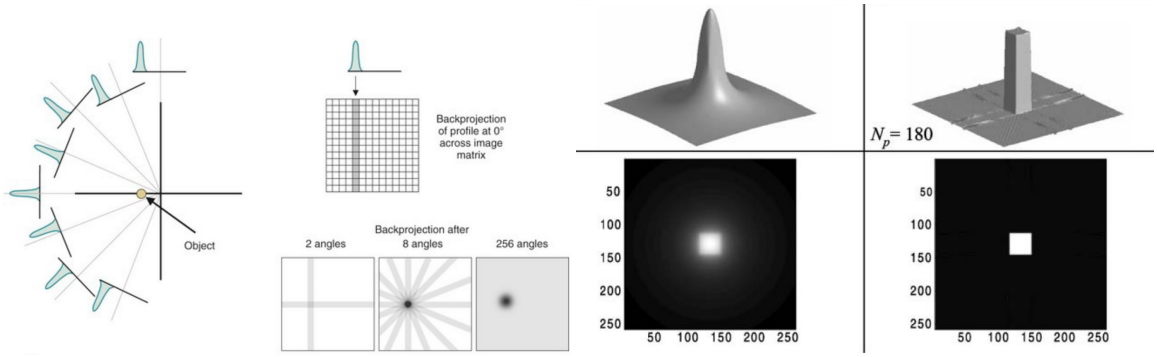

Fig 4 Schematic illustration of the simple backprojection principle and on the right hand side a comparison of a corresponding result with the result of the broadly utilized filtered backprojection reconstruction for a slice of an object with a squared cross section;

However, reconstruction can be done in many ways particularly also through iterative algorithms, which are especially useful for limited data sets and limited data quality. In addition, different beam conditions, such as cone beam geometries or the spatial resolved reconstruction of different parameters require different approaches and a departure from some of the fundamental concepts utilized here. This would be the case e.g. for the reconstruction of vectorial entities instead of scalars. In addition, strictly considered, neutron imaging experiments rather use conic beams, where the independent slice approach is not fully supported. However, within the spatial resolutions utilized normally the parallel beam proves generally a sufficient approximation.

2 Neutron Imaging - Contrast

The second indispensible ingredient for imaging, besides the spatial resolution, is contrast. Here the picture changed significantly within the past one or two decades, adding contrast modalities far beyond the conventional wavelength integrated neutron attenuation [1,14-16]. The basic concepts of contrast with neutrons will, however, be outlined along the lines of this conventional, initial and still dominating contrast modality, which lends its strengths from the most unique characteristics of neutron radiation. It has to be noted that referring here to neutron radiation shall be restricted to the range of thermal and cold neutrons. This does not mean that other regimes, especially of higher energy neutrons are not utilized for imaging. They are. And higher energies even increase the material volumes that can be penetrated,

however, in turn the resolution and particularly the detector efficiency suffer severely. Nevertheless, beyond the mainstream useful applications have also been demonstrated, most notably lately element, isotope and temperature sensitive neutron imaging utilizing resonance absorption [17].

The unique fundamental features of neutron radiation outlined in the introduction imply their value for application in radiographic imaging despite the issues with focussing, flux and spatial resolution stressed in the previous section. The specific characteristics of neutrons in the interaction with matter play a key role in the application of neutron imaging (just as much as in scattering) and most of them are key drivers for conventional attenuation contrast imaging as well, as is illustrated also in Fig. 5.

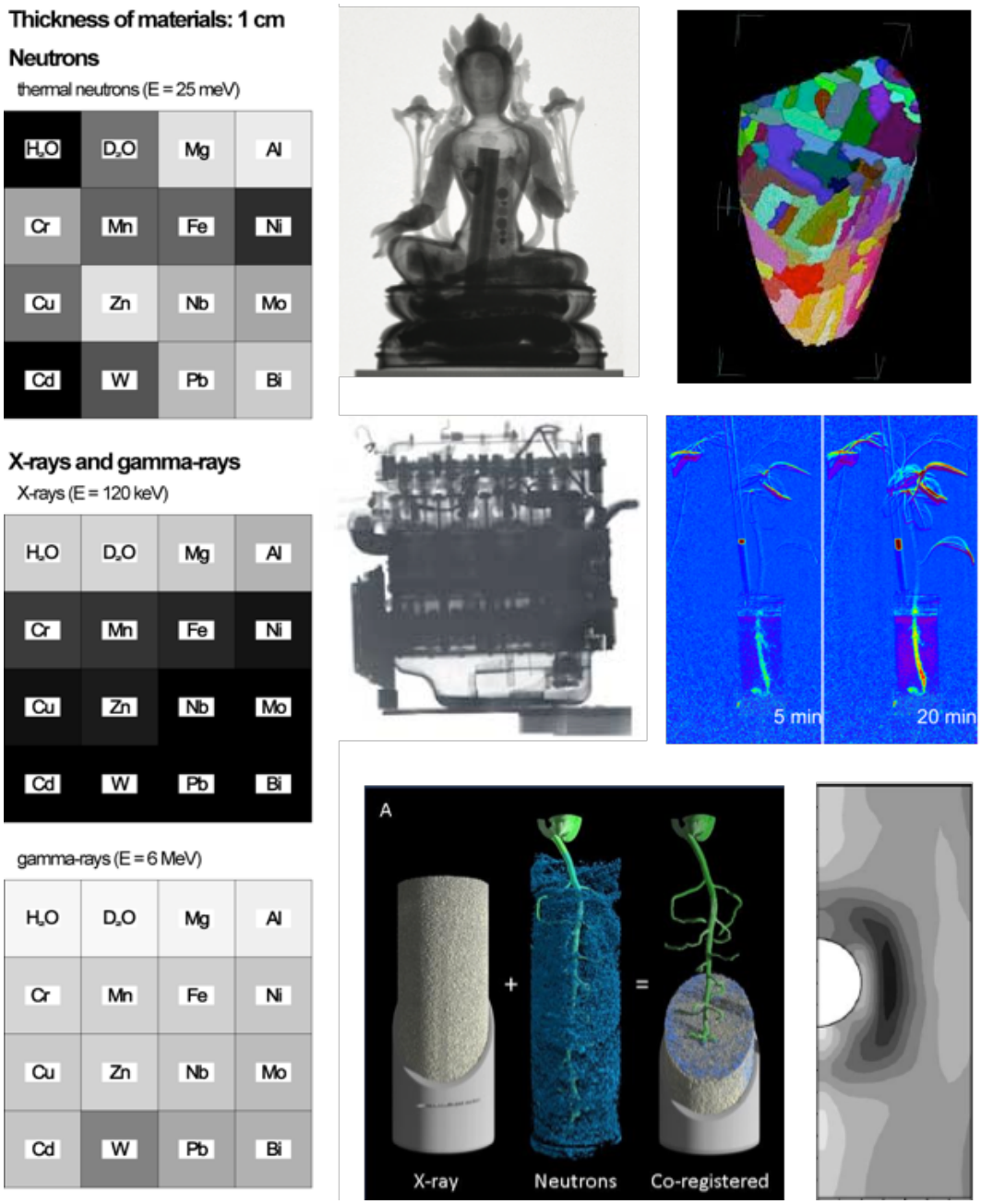

Fig. 5 left hand side: comparison of neutron attenuation contrast with x-rays and gamma rays of certain energies; the scattered contrast and significant differences between

elements close in the periodic tabble in contrast to photons is illustrated; right hand side from left to right and top to bottom: attenuation contrast neuton image of cultural heritage object utilizing the ability of neutrons to transmit the metallic sculpture and still being highly sensitive to hydrogeneous organic material inside, enabling their non-destructive study; dark-field contrast neutron tomography displaying the magnetic domain network in the bulk of an FeNi crystal, where it is not amenabble by any other technique [18]; attenuation contrast neutron image of a whole BMW motor block, with neutrons still being sennsitive to the oil distribution inside; two slices of a time resolved attenuation contrast neutron imaging study utilizing D_2O/H_2O contrast to study the wateruptake of a plant; study of the interactions in a root-soil-water system through bi-modal simultaneous neutron and x-ray tomography, where the x-rays better resolve the soil structure, while neutrons provide better contrast for water and root; diffraction contrast neutron image providing a through plane strain map around a cold expanded hole of 1 cm diameter in steel [19];

In order to correctly detect an image $I(x,z)$ based on the contrast provided by the sample the measured image $I_m(x,z)$ has to be background corrected by an image $I_{bg}(x,z)$ and normalized by the incident beam profile measured as $I_0(x,z)$, according to

$$I(x,z) = (I_m(x,z) - I_{bg}(x,z))/(I_0(x,z) - I_{bg}(x,z)) \quad (8)$$

Note that $I_0(x,z)$ does not always have to be an open beam, or so-called flat-field image, but e.g. when observing changes over time, it can be very useful to normalize with the image of the initial state at time $t = 0$ (compare images Fig. 5 mid row, right hand side). Note further, that the background image can contain a significant number of constituents, starting from the discussed detector read-out noise and might even contain biasing contributions from the sample itself. Correction strategies in particular for measurements requiring an extensive level of quantification are not limited to simple or more sophisticated measurements, but are sometimes including complex correction algorithms [20].
(In the following sections in equations, image notation will assume background not further relevant and will be simplyfied accordingly, if not locally stated differently.)

2.1 Attenuation contrast

Attenuation is often wrongly referred to as absorption in imaging. However, in particular in cold and thermal neutron imaging scattering contributions are in many cases dominating the measured attenuation contrast. The entity providing contrast and hence measured is referred to as the linear attenuation coefficient $\mu = N\sigma_{tot} = N(\sigma_a + \sigma_s)$ and correspondingly is based on the total microscopic cross section σ_{tot}, which is the sum of the microscopic absorption σ_a and scattering cross section σ_s. With N being the particle density the linear attenuation coefficeint has the unit of a length, generally given in cm^{-1}. Therefore the total contrast measured with respect to the incident beam depends also on the material thickness and the equation constituting an image is a two dimennsional version of the Beer Lambert law

$$I(x,z) = I_0(x,z)e^{-\int \mu(x,y,z)dy} \quad (9)$$

and consequently the relevant projection image will rather read

$$P(x,z) = -\ln\frac{I(x,z)}{I_0(x,z)} = \int \mu(x,y,z)dy \tag{10}$$

A number of example images as well as contrast to be expected for different elements are displayed in figure 5. However, only one 3D example is shown, only four out of the six images are conventional attenuation contrast images and the data presented is more or less heavily processed. Apart from the introduced backgrounnd correction, in many cases imaging data requires further processing through filtering as it is affected e.g. by Poisson noise in the counting statistics, and e.g. tomographic reconstruction can amplify biases. Sophisticated filtering operation are hence often key for good results but operate at the edge of resolution diluation and bias. Fig. 6 nicely illustrates differennt filter attempts and a successful filter operation on a tomographic slice (Fig. 6 left).

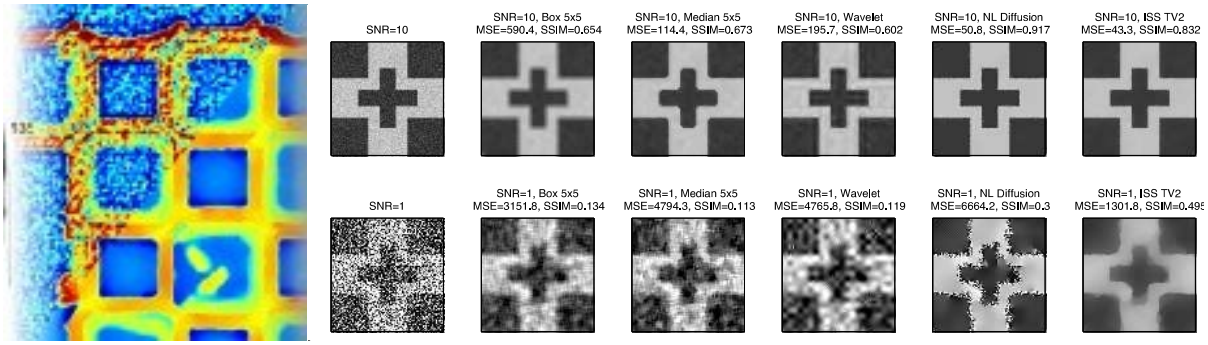

Fig. 6 Initial image quality and filtered result in a tomographic slice of a diesel particulate filter ob the left; various image filtering examples for initial images of different statistical quality;

In general the images produced and presented here are, however, still intermediate results, and processing to get these can be regarded data reduction processes, but the actual analyses is still to come. In contrast to scattering techniques, which continuously produce similar results and data sets, which are fitted with similar models, always looking at the same kind of problem, the situation is significantly different in imaging, where depending on the image and sample, the features to be extracted from conventional attenuation contrast images can be as different as the identification of a single failure in a component in non-destructive testing, to detailed structural analyses and modelling of processes in material science similar to any other material science characterisation technique, including neutron scattering (compare Fig. 1).

However, the application of a broad spectrum in favor of a high flux for high resolution imaging implies potential bias to quantification based on the attenuation coefficient. The energy dependence of $\mu(x,y,z,E)$ does not only imply that the applied energy spectrum has to be taken into account in any quantification of the attenuation coefficient distribution, but also, that significant variations with the energy can lead to effects similar to what is known as beam hardening in x-ray imaging, were penetration increases toward harder, higher energy, radiation. In imaging with neutrons in the thermal and in particular cold energy range, a very peculiar wavelength dependence (in modern neutron imaging the characterisation by wavelength replaces the characterisation through energy) characterizes the transmission spectra of crystalline materials (with high coherent scattering cross sections). Applying wavelength resolved imaging, this specific diffraction related feature can be exploited in what

is refered to as diffraction contrast [14]. Eventually, it makes imaging kind of just another scattering technique (Fig. 7 right), but operating with intirnsic real space resolution.

2.2 Diffraction contrast – Bragg edges

Recalling that the attenuation contrast is based on the sum of the absorption and scattering cross sections it is worthwhile particularly for crystalline materials to have a closer look into the contributions to the scattering cross section for cold and thermal neutrons (Fig. 7). The scattering cross section can further be broken down according to different interaction characteristics into coherent and incoherent as well as into elastic and inelastic contributions providing the options of coeherent elastic (Fig. 7 black) and coherent inelastic (Fig. 7 red) as well as incoherent elastic and incoherent inelastic scattering (Fig. 7 green and blue) contributions.

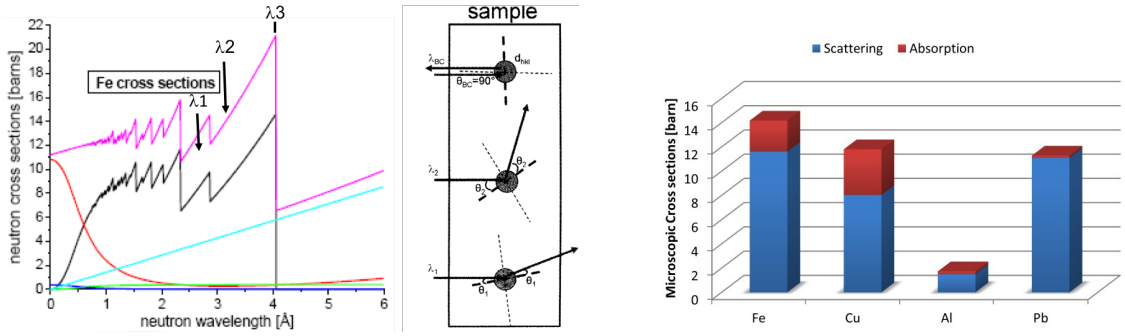

Fig. 7 Different contributions to the total neutron cross section (magenta) depending on neutron wavelength focussing on the cold and thermal energy range, using Fe as an example with a dominating part of coherent elastic (Bragg) scattering (black line); mid schematic together with left hand side graph illustrate the principle of the Bragg edges in the cross section; right hand side: scattering versus absorption contributions for four important metallic materials;

Fig. 7 left side depicts the individual contributions for iron, and it can be seen that in this case the coherent elastic cross section, through the distinct Bragg scattering, dominates the attenuation in the thermal and cold range up to around 4 Å. The turquoise line representing the absortion cross section is dominating beyond this point with a linear growing tendency with increasing wavelength (decreasing energy), while the mangenta line is the sum of all contributions. The coherent elastic Bragg scattering induces a distinct pattern characterised by well defined Bragg edges. The middle figure 7 is to illustrate the principle causing the Bragg edge pattern. At a specific hkl lattice plane family neutrons of a certain wavelength can deflect only at certain orientations of the lattice to the beam according to Bragg's law

$$\lambda = 2d_{hkl} \sin\theta \tag{11}$$

which implies that above a certain wavelength $\lambda = 2d_{hkl}$ where the Bragg angle is $\theta = \pi/2$ no more Bragg scattering can take place for wavelengths longer than two times the specific lattice distance d_{hkl}, and hence the transmission increases steeply beyond that point in the spectrum.

This, however, implies, that there is significant crystallographic information encoded in the transmission spectra, which can be exploited with spatial resolution through wavelength resolved attenuation contrast imaging, providing diffraction contrast [14].

Instrumental attempts to do so are manifold. At continuous sources velocity selctors and double crystal monochromators are utilized for low (around $d\lambda/\lambda$ 10%) and medium (around $d\lambda/\lambda$ 3%) wavelength resolution in conventional imaging instruments, respectively. The utilisation of time-of-flight for imaging has been explored at conntinuous and pulsed sources, at the latter in particular for high wavelength resolutions $d\lambda/\lambda$ below 1%.

Applications convey quantitative investigations of phase fractions and phase transformation with 2D and 3D spatial resolution as well as strain mapping with latest attempts proving the principle feasibility of strain tomography. In addition, spatial varitions of texture can be visualised and grain size analyses has been attempted. In Fig. 5 in the bottom right corner the first successfully measured strain map around a cold expanded hole (10mm diameter) in an 12mm thick ferritic steel plate is presented. The grey scale is spread from strains below 0 being white and above 900 microstrain being black [19].
Strains and phases can be evaluated particularly for powder like samples with random grain orientations. Strains are characterized by small shifts of Bragg edges. To measure such, good wavelength resolution is required. This resolution can be relaxed for phases, which can be quantified based on edge heights. Measurements of two discrete wavelengths, sometimes even a single monochromatic measurement, are hence sufficient for the latter, while the edge analyses for strain requires detailed sampling of edges. In the case of texture the distinct Bragg edge pattern characteristic of a crystal structure vanishes depending on the degree of texture as can be seen in the middel graph in Fig. 8 top. Finally very large grains, within the spatial resolution of the imaging set-up (around 100 μm), show the signature of discrete Bragg peaks rather than a Bragg edge structure. These patterns (Fig. 8 top right) can be used in tomographic approaches to reconstruct the grain network and morphology of a sample (Fig. 8 bottom right) [21].

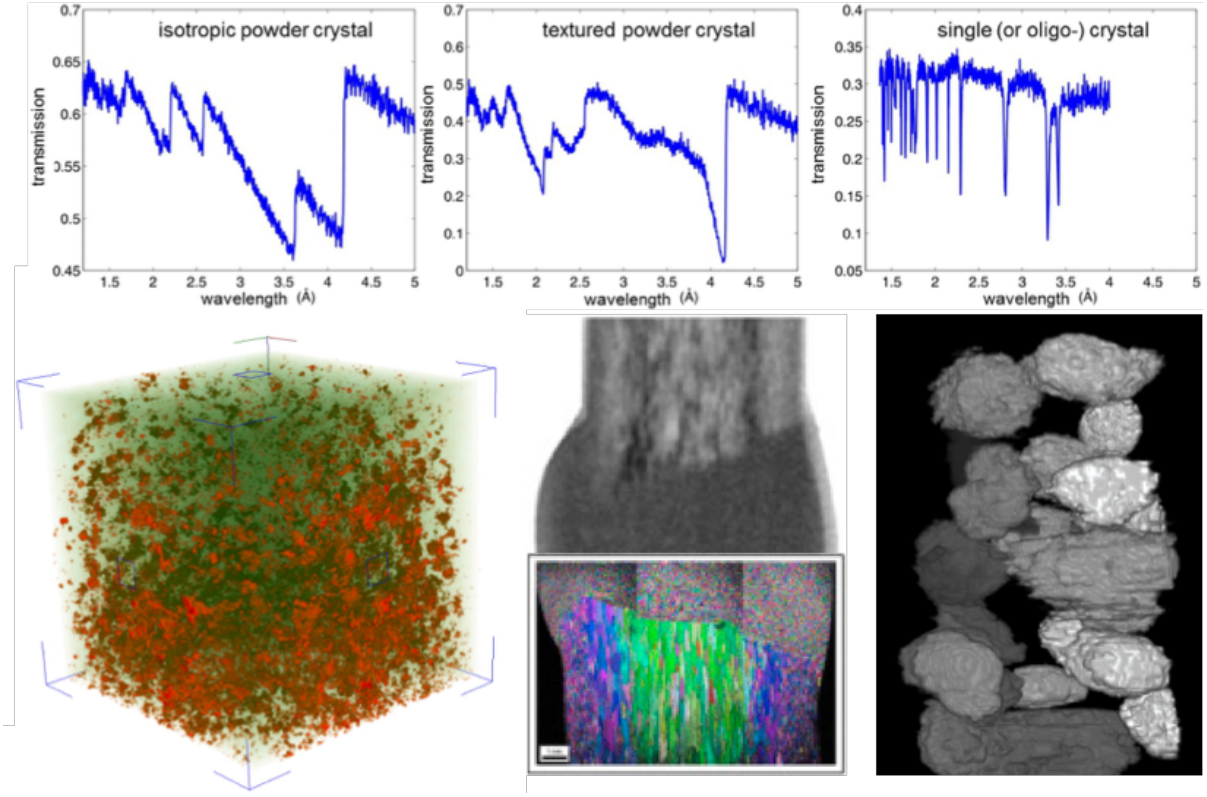

Fig. 8 Top: transmission spectra illustrating 3 distinct cases of powder like random oriented small grained crystallic samples, similar but textured samples and with grain sizes within the range of direct spatial resolution of the imaging set-up annd hence limited number of grains; Bottom: application examples convey mapping of crystalline phases (here mix of α and γ phase in steel in 3D), varying grain structure in a weld of rolled steel and single grains in an Fe sample reconstructed tomographically [21];

2.3 Dark-field contrast – Small angle scattering

Dark-field contrast can be achieved, when an imaging set-up is sensitive to small angle scattering. Nowadays this is realized through spatial modulation of the full extended beam utilized for imaging [15]. Spatially resolved small angle scattering is then detected by local losses of the modulation visibility V [22], which is defined as

$$V=(I_{max}-I_{min})/(I_{max}+I_{min}) \quad (12)$$

Different approaches exist to induce and detect spatial beam modulation and in particular its visibility [15]. The utilized modulation period p has a key influence on the scattering vector range probed and whether it is ranging in the ultra-small, very-small or small angle scattering range [15,23]. Tthe smallest modulations are produced in the micrometer range and are hence beyond the spatial resolution of the imaging set-up. Therefore such modulations have to be measured and analysed within every individual pixel. This is normally achieved with analyser gratings with the period of the modulation, and a scan of these enables the step-wise visualistation of the modulation in each pixel. If the modulation is spatially resolved, then it is superimposed to the attenuation image, and the spatial resolution of the small angle scattering information is limited by the modulation period [24].

Micrometer sized modulation periods are realized with Talbot-Lau grating interferometers, and larger periods e.g. in so-called far-field grating interferometers, using Moire fringes and even Spin-Echo devices [15,24].

Even applications not quantifying the small angle scatter signal have proven very use- and successful not only to detect structural variation but in particular magnetic domain walls, which can be directly visualized. Fig. 5 top right shows the first ever observation of bulk magnetic domains through the application of dark-field contrast neutron tomography [18].

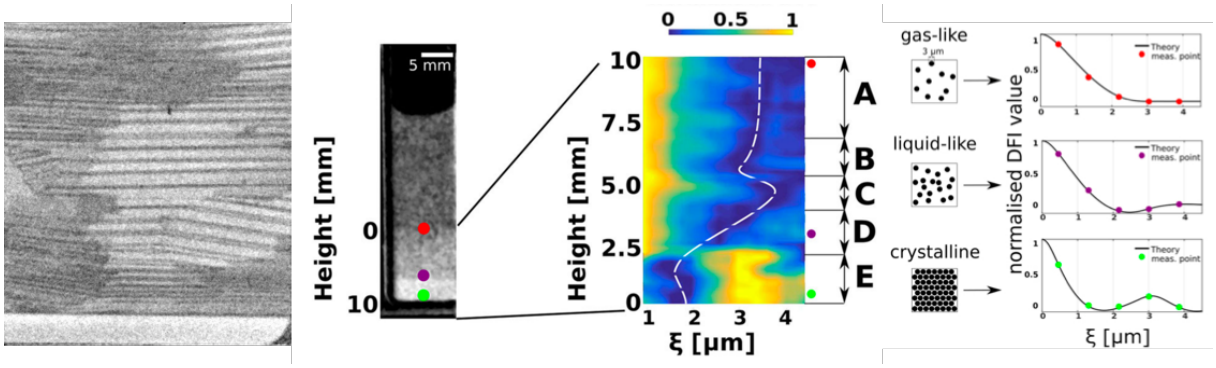

Fig. 9 left: magnetic domain walls in GOSS oriented steel used in transformers [25], mid to right: height resolved different phases in a system of mircospheres diluted in an H_2O/D_2O mixture and forming a crytal-like phase when sedimenting on the bottom of the imaged cuvette [26];

However, dark-field contrast is also suited to quantify small angle scattering and hence structures in the micro- to nanometer regime, beyond direct spatial resolution of neutron imaging. The particular correlation length ξ probed in a measurement can be described as [23]

$$\xi = \lambda L_s / p \tag{13}$$

and hence depends apart from the period p also on the utilized wavelength and the sample to detector/analyser grating distance L_s. When the period is fixed (like in grating set-ups in contrast to magnetic set-ups in spin-echo) the wavelength and to some extend the distance (note, with corresponding impact on spatial image resolution) are appropriate parameters to alter ξ in order to scan a specific correlation length range. Correlation length ranges beyond one order of magnitude have been reported within boundaries of some 10 nm up to nearly 10 µm [15].

Small angle scattering structures can pixel-wise or within the spatial resolution of the image be characterised due to the relation [23]

$$V(\xi,x,z)\Big/_{V_0(\xi,x,z)} = e^{\int \Sigma_s(x,y,z)(G(\xi,x,y,z)-1)dy} \tag{14}$$

Here V_0 is the visibility of the modulation without sample, Σ_s is the small angle scattering cross section based on the scattering length density contrast of the materials and the density of

the scattering structures as well as the wavelenth square. $G(\xi)$ a projected real space correlation function of the scattering structure containing the morphology information [23]. Note that this correlation function is reduced to one dimension according to the currenntly used modulation techniques being sensitive in one dimension only, comparable to slit-smeared small angle instruments. In contrast to small angle scattering instruments, here measurements remain in real space, because the modulation technique constitutes a backprojection from Fourier to real space according to [23]

$$V_s(\xi, q) = V_0(\xi) \int_{-\infty}^{\infty} dq\, S(q)\, cos(\xi q) \tag{15}$$

where $S(q)$ is the small angle scattering function and q the modulus of the scattering vector.

Applications are in the study of structures and structural developments which are not homogeneous throughout the sample volume as required in conventional SANS. Fig. 9 provides a few examples of dark-field contrast imaging, including one exploiting the spatial resolved quantitative SANS evaluation.

2.4 Polarisation contrast – Spin precession

The sensitivity of neutrons to magnetic fields and structures is one of the main applications in neutron science and in particular neutron scattering. However, this specific feature can also be exploited in spatially resolved polarized neutron imaging studies in the macroscopic domain [16, 27]. While examples have already been shown with respect to dark-field contrast, polarisation contrast utilizes polarisation analyses and spin precession in order to visualize and analyse magnetic structures and fields. The basic principle of polarized neutron imaging builts on the Larmor precession of the neutron spin when traversing a magnetic field.

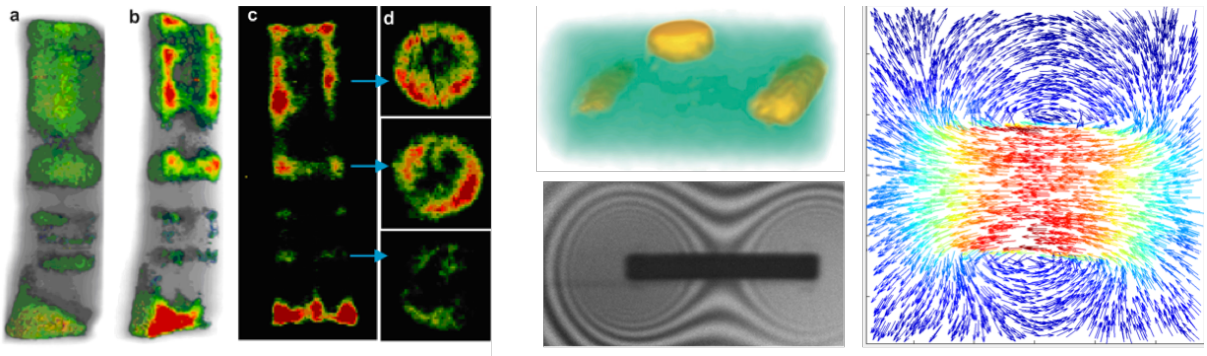

Fig. 10 left: Curie temperature mapping through depolarisation imaging, providing 3D maps of the already ferromagnetic parts of a sample at a certain temperature [16]; mid top: 3D reconstrcution of magnetic field areas trapped in a lead superconductor close to the critical temperature [27]; mid bottom: straightforward polarized neutron radiography of the field of a dipol magnet [28] and right hand side: a result of the first 3D magnetic field reconstruction from a polarimetric neutron tomography (color indicates field strength)[29];

The spin precession of the polarisation vector **P** around a magnetic field vector **B** can be expressed by

$$\frac{d\boldsymbol{P}}{dt} = \gamma \boldsymbol{P} \times \boldsymbol{B} \tag{16}$$

and hence the accumulated rotation angle

$$\varphi = \omega_L t = \frac{\gamma}{v} \int_{path} B ds = \frac{\gamma m \lambda}{h} \int_{path} B ds \tag{17}$$

where $\gamma = -4\pi\mu/h = 1.832\ 10^8$ rad/s/T being the gyromagnetic factor of the neutron, with h being the Planck constant. *v* denotes the velocity of the neutron and *m* its mass. Utilizing a polarized incident beam and a polarisation analyser between sample and detector and for illustration assuming a magnetic field perpendicular to the polarisation of the beam the signal in the resulting image can be described by

$$I(x,y) = I_0(x,y) \exp\left(-\int \Sigma(s) ds\right) (1 + cos\varphi)/2 \tag{18}$$

and when normalised for the attenuation simply

$$I(x,y) = I_0(x,y)(1 + cos\varphi)/2 \tag{19}$$

This enables a visualisation, but a quantification only for simple cases, sufficient a priori knowledge or significant field modelling efforts. Nevertheless the detection of magnetic field variations in the bulk of materials, where it is not amenable to any other technique has proven useful. In addition, more complex techniques have developed and meanwhile the 3D reconstruction of magnetic vector fields has become possible. Also simple implementations, not striving for reconstructing the field distribution but to detect e.g. the phase transition from paramagnetic to ferromagnetic at the Curie temperature simply probing depolarisation turned out interesting for numerous applications as well. Fig. 10 provides examples of different complexity and applications.

References

[1] M. Strobl, N. Kardjilov, A. Hilger, I. Manke, J. Banhart, Topical Review: Advances in neutron radiography and tomography, J. Phys. D 42 (2009) 243001.

[2] N. Kardjilov, I. Manke, A. Hilger, M. Strobl, J. Banhart, Neutron imaging in material science, Materials Today, 14(6) (2011) 248–256.

[3] Hickner M A, Siegel N P, Chen K S, Hussey D S, Jacobson D L and Arif M, Understanding liquid water distribution and removal phenomena in an operating PEMFC via neutron radiography J. Electrochem. Soc. 155 (2008) B427.

[4] J. Biesdorf, P. Oberholzer, F. Bernauer, A. Kaestner, P. Vontobel, E. H. Lehmann, T. J. Schmidt und P. Boillat, Dual spectrum neutron radiography: Identification of phase transitions between frozen and liquid water, Physical Review Letters 112, 24 (2014) 248301.

[5] I. Manke, Ch. Hartnig, N. Kardjilov, M. Messerschmidt, A. Hilger, M. Strobl, W. Lehnert, J. Banhart, Characterization of water exchange and two-phase flow in porous gas diffusion materials by H-D contrast neutron radiography, Appl. Phys. Lett. 92, 244101 (2008).

[6] A. Bazylak, Liquid water visualization in PEM fuel cells: a review, International Journal of Hydrogen Energy 34, 9 (2009) 3845-3857

[7] D.F.R.Mildnera, M.V.Gubarev, Wolter optics for neutron focusing, Nucl. Instr. Meth. A 634, 1 (2011) 7-11.

[8] O. H. Siegmund, J. V. Vallerga, A. S. Tremsin, J. Mcphate and B. Feller, High spatial resolution neutron sensing microchannel plate detectors Nucl. Instrum. Methods A 576 (2007)178.

[9] P. Trtik, E. Lehmann, Isotopically-enriched gadolinium-157 oxysulfide scintillator screens for the high-resolution neutron imaging, NIM-A, 788 (2015) 67-70.

[10] P.Trtik, E. Lehmann, Progress in high-resolution neutron imaging at the Paul Scherrer Institut – The Neutron Microscope project, Journal of Physics - Conference Series, 746 (2016) 012004.

[11] M. Morgano, P. Trtik, M. Meyer, E. H. Lehmann J. Hovind and M. Strobl, Unlocking high spatial resolution in neutron imaging through an add-on fibre optics taper, Optics Express 26, 2 (2018) 1809.

[12] Radon J 1917 Ber. Saechsischer Akad. Wiss. 29 262.

[13] A.P. Kaestner, MuhRec - a new tomography reconstructor, NIMA 651, 1 (2011). software: https://www.psi.ch/niag/muhrec

[14] R. Woracek, J. Santisteban, A. Fedrigo, M. Strobl, Diffraction in neutron imaging—A review, Nucl. Inst. Meth. A 878 (2018) 141–158.

[15] M. Strobl, R. P. Harti, C. Grünzweig, R. Woracek, J. Plomp, Small Angle Scattering in Neutron Imaging—A Review, J. Imaging 3 (2018) 64.

[16] M. Strobl, H. Heimonen, S. Schmidt, M. Sales, N. Kardjilov, A. Hilger, I. Manke, T. Shinohara, J. Valsecchi, Jacopo Topical review: Polarisation measurements in neutron imaging, J. Phys. D, in the press.

[17] A. S. Tremsin, J. B. McPhate, J. V. Vallerga, O. H. W. Siegmund, W. Kockelmann, E. M. Schooneveld, N. J. Rhodes, W. Bruce Feller, High Resolution Neutron Resonance Absorption Imaging at a Pulsed Neutron Beamline, IEEE Transactions on Nucl. Sci. 59, 6 (2012).

[18] I. Manke, N. Kardjilov, R. Schäfer, A. Hilger, M. Strobl, M. Dawson, C. Grünzweig, G. Behr, M. Hentschel, C. David, A. Kupsch, A. Lange, J. BanhartThree-dimensional imaging of magnetic domains, Nature Commun. 1, 125 (2010).
[19] J.R. Santisteban, L. Edwards, M.E. Fitzpatrick, A. Steuwer, P.J. Withers, M.R. Daymond, M.W. Johnson, N. Rhodes, E.M. Schooneveld, Strain imaging by Bragg edge neutron transmission, Nucl. Instr. Meth. A 481 (2002) 765–768.
[20] P. Boillat, C. Carminati, F. Schmid, C. Grünzweig, J. Hovind, A. Kaestner, D. Mannes, M. Morgano, M. Siegwart, P. Trtik, P. Vontobel, and E.H. Lehmann, Chasing quantitative biases in neutron imaging with scintillator-camera detectors: a practical method with black body grids, Optics Express 26, 12, (2018) 15769-15784.
[21] A. Cereser, M. Strobl, S. A. Hall, A. Steuwer, R. Kiyanagi, A. S. Tremsin, E. B. Knudsen, T. Shinohara, P. K. Willendrup, A. Bastos da Silva Fanta, S. Iyengar, P. M. Larsen, T. Hanashima, T. Moyoshi, P. M. Kadletz, P. Krooß, T. Niendorf, M. Sales, W. W. Schmahl, and S. Schmidt
Time-of-Flight Three Dimensional Neutron Diffraction in Transmission Mode for Mapping Crystal Grain Structures, Scientific Reports 2017; 7: 9561.
[22] M. Strobl, C. Grünzweig, A. Hilger, I. Manke, N. Kardjilov, C. David, F. Pfeiffer, Neutron dark-field tomography, Phys. Rev. Lett. 101, 123902 (2008).
[23] M. Strobl, General solution for quantitative dark-field contrast imaging with grating interferometers, Scientific Reports 4 (2014) 7243.
[24] M. Strobl, M. Sales, J. Plomp, W. G. Bouwman, A. S. Tremsin, A. Kaestner, C. Pappas, K. Habicht, Quantitative Neutron Dark-field Imaging through Spin-Echo Interferometry, Scientific Reports, 5, 16576 (2015).
[25] R. P. Harti, M. Strobl, R. Schäfer, N. Kardjilov, A. S. Tremsin & C. Grünzweig, Dynamic volume magnetic domain wall imaging in grain oriented electrical steel at power frequencies with accumulative high-frame rate neutron dark-field imaging, Scientific Reports 8, 15754 (2018).
[26] R. P. Harti, M. Strobl, B. Betz, K. Jefimovs, M. Kagias, C. Gruenzweig, Sub-pixel correlation length neutron imaging: Spatially resolved scattering information of microstructures on a macroscopic scale, Scientific Reports 7:44588 (2017).
[27] N. Kardjilov, I.Manke, M. Strobl, A. Hilger, W. Treimer, M. Meissner, T. Krist, J. Banhart
Three-dimensional imaging of magnetic fields with polarized neutrons, Nature Physics, 4 (2008).
[28] M. Strobl, N. Kardjilov, A. Hilger, E. Jericha, G. Badurek, I. Manke, Imaging with polarized neutrons, Phys. B 404 (2009) 2611–2614.
[29] M. Sales, M. Strobl, T. Shinohara, A. Tremsin, L. Theil Kuhn, W. Lionheart, N. Desai, A. Bjorholm Dahl, and S. Schmidt, Three Dimensional Polarimetric Neutron Tomography of Magnetic Fields, Scientific Reports 8, 2214 (2018).